Carbon 221 (2024) 118940

Contents lists available at ScienceDirect

Carbon

journal homepage: www.elsevier.com/locate/carbon

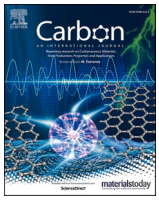

# High surface area microporous carbon nanocubes from controlled processing of graphene oxide nanoribbons

Saeed Khodabakhshi [a,*], Pasquale F. Fulvio [b], Krista S. Walton [b], Sajad Kiani [a], Yubiao Niu [c], Richard E. Palmer [c], Andrew R. Barron [a,d,e,f], Enrico Andreoli [a,**]

[a] Energy Safety Research Institute, Swansea University, Bay Campus, Swansea, SA1 8EN, UK
[b] Department of Chemical and Biomolecular Engineering, Georgia Institute of Technology, Atlanta, GA, 30318, USA
[c] Nanomaterials Lab, Mechanical Engineering, Swansea University, Bay Campus, Swansea, SA1 8EN, UK
[d] Arizona Institute for Resilience (AIR), University of Arizona, Tucson, AZ, 85721, USA
[e] Department of Chemistry and Department of Materials Science and Nanoengineering, Rice University, Houston, TX, 77005, USA
[f] Faculty of Engineering, Universiti Teknologi Brunei, Brunei Darussalam

ARTICLE INFO

*Keywords:*
Nanocubes
Carbon black
Nanoribbons
$CO_2$ capture
Microporous carbon

ABSTRACT

A new, facile, and template-free method to prepare high surface area microporous carbon nanocubes (CNCs) from a mixture of graphene oxide nanoribbons (NRs), graphene oxide, and carbon dots is reported. The nanoribbons, approximately 30 nm wide and with lengths ranging from a few tens of nanometres up to several micrometres, were obtained from the oxidation of Black Pearls 2000 carbon black in nitric acid solution. The non-purified nanoribbons further contained additional fragments of graphene oxide, and of graphene oxide quantum dots. Slow pyrolysis of the nanoribbon mixture with slow heating rates, e.g., 3 °C/min, yielded carbon nanocubes approximately 250 nm in size with surface areas greater than 900 $m^2/g$. Heating rates of 50 °C/min led to carbons with ~800 $m^2/g$ surface area but bulk morphology. Precipitating the nanoribbons in potassium hydroxide solution, followed by carbonization, yielded microporous nanoparticle aggregates that were 20 nm in size with surface areas greater than 2000 $m^2/g$. The particles exhibited complex, quasi-spherical morphology. Pyrolysis of other products obtained from oxidation in $HNO_3$ of different grades of carbon black, specifically graphene oxide nanoparticles and quantum dots, yielded high surface area microporous carbons but with bulk morphology regardless of the processing conditions. Despite the lower surface area and pore volume of the CNCs in comparison to the nanospheres, the former contained ultramicropores that were highly accessible to $CO_2$ as a molecular probe and had excellent selectivity of $CO_2$ over $N_2$. Hence, CNC materials have promising properties for applications where particle surface-to-volume ratios, high internal surface areas, and abundant super and ultramicropores are desired.

## 1. Introduction

Porous carbons find many technological applications; these are commonly obtained industrially from abundant biomass precursors that are shaped into granular form and used as sorbents for air and water purification [1,2]. Such carbons, however, require physical or chemical activation methods to yield micro and mesopores. At the micro and nanoscales, the particle morphology cannot be controlled, thus restricting diffusion into the internal particle pores [3–5]. On the other hand, nanosized carbons, such as carbon nanospheres (CNSs) exhibit unique properties that are of interest to separations, carbon capture, energy storage and biomedical applications [1,2,6–9]. Compared to CNS materials, the less investigated carbon nanocubes (CNCs) also display promising properties for different technological uses including drug delivery [10], electronic devices [11,12], sensors [13], energy storage and conversion [14–21], and heterogeneous catalysis [22].

To date, CNCs have been prepared by pyrolysis of metal-organic frameworks (MOFs), such as cubic nanocrystals of zinc imidazolate framework (ZIF-8) [10,15,22] and Prussian Blue derivatives [12,14,18,19]. Of these, materials prepared from pyrolysis of

* Corresponding author.
** Corresponding author.
*E-mail addresses:* Saeid.khodabakhshi@swansea.ac.uk (S. Khodabakhshi), E.Andreoli@Swansea.ac.uk (E. Andreoli).

https://doi.org/10.1016/j.carbon.2024.118940
Received 19 November 2023; Received in revised form 2 February 2024; Accepted 14 February 2024
Available online 14 February 2024

polydopamine-encapsulated iron (Fe) and cobalt (Co) containing hexacyanoferrate yielded FeCo@CNCs were highly conductive, with electrical conductivity matching that of graphite (~1200 S/m). The latter was also found to be selective catalysts for the oxygen reduction reaction [8]. Co-hexacyanoferrate nanocubes of approximately 80 nm in size have also been grown in the presence of excess polyvinylpyrrolidone (PVP), and the FeCo@CNCs were obtained after carbonization. Carbon tubes formed without the PVP, whereas small amounts of PVP lead to random carbon nanoparticle aggregates. Interestingly, the FeCo@CNCs were found more active than tubes and aggregated particles for the iodide oxidation in dye-sensitized solar cells (DSSCs). Results were due to the high surface area to volume ratio of catalysts, good electrical conductivity and the microporous-mesoporous structure of FeCo@CNCs [14]. Direct carbonization of Prussian Blue (PB) nanocubes also resulted in CNCs with low specific surface areas (45–70 $m^2/g$) that were as large as 700 nm. The presence of metallic Fe encapsulated by a graphitized carbon shell rendered these Fe@CNCs good microwave absorption properties [12]. Moreover, Fe-free CNCs from PB cubic crystals carbonization and with sizes ranging from 500 nm to 700 nm were obtained after hydrochloric acid (HCl) dissolution. Tungsten disulphide ($WS_2$) nanopetals were then grown over the CNCs and final composites were tested as anodes for sodium-ion batteries (SIBs). The nanocomposites retained most of their capacities at high charge-discharge rates and exhibited excellent stability up to 200 cycles [19]. CNC composites were also obtained from the carbonization of cubic ZIF-8 nanocrystals. The cubic morphology of the precursor was controlled by mixing cetyltrimethylammonium bromide (CTAB) surfactant. The resulting crystals were carbonized in two steps, between which selenium (Se) was added, and microporous ZnSe–CNCs of 250 nm in size and with surface areas exceeding 700 $m^2/g$ were obtained. The latter was tested as anodes in lithium-ion batteries (LIBs), displaying high discharge capacity and greater than 60% Coulombic efficiency [15]. When Zn was partially etched from the cubic ZIF-8 crystals with tannic acid, double shell ZnO@CNC structures formed. These nanocomposites had large mesopores and were excellent sorbents for the removal of benzene, toluene, ethylbenzene and xylene (BTEX) compounds from water to levels below the detection limit of gas chromatography (GC) [21]. Silica-coated CNCs were prepared by coating ZIF-8 with and hydrolysing $SiO_2$ precursor, followed by carbonization. The composites were then coated with polyacrylic acid (PAA) and tested for drug delivery. The final $SiO_2$–CNC nanocomposites were approximately 120 nm in size, had a $SiO_2$ shell of 25 nm, mesopores of 8 nm width and surface areas greater than 540 $m^2/g$ [10]. Besides ZIF-8, a mesoporous Zn-based squaric acid MOF was prepared and carbonized. After etching the Zn with acid, carbon cubes with micron size, the hierarchical pore structure of micro, meso and macro-pores and with surface areas of 1200 $m^2/g$ were obtained. When tested as supercapacitor electrodes, capacitance values were as high as 133 F/g in the aqueous sulfuric acid electrolyte, which is comparable to most porous carbon electrodes. Despite the micron-scale size of the precursor and resulting carbon particles, this route is promising for further developments of MOFs and MOF-derived carbons for electrochemical applications [21].[21]

CNC-ceramic composites have been prepared by ball-milling paraffin wax, octadecylamine and the precursors to $Na_3V_2(PO_4)_2F_3$, followed by carbonization [16]. The composites had quasi-cubic morphology and other desired properties promising for applications as SIB electrodes due to their fast $Na^+$ diffusion capability, with 107 mAh/g discharge capacity at rates as fast as 30 C and 84% capacitance retention over 2500 cycles. Other additives such as stearic acid led to the formation of nanorods, whereas Span 80 nonionic surfactant induced the formation of a nanoflake morphology [16]. Another interesting route for porous CNCs was the precipitation of cubic manganese acetate nanocubes into $MnCO_3$. The carbonate phase was then calcined in air at 600 °C. The resulting product was mesoporous MnO nanocubes. Then, carbon was grown over the MnO support by chemical vapor deposition of acetylene gas at 750 °C. After etching of the MnO, a highly porous CNC with a surface area >2500 $m^2/g$ and particle size of 600 nm was obtained. The large mesopores served as reservoirs for sulphur in Li-sulphur batteries [17]. Besides self-templated strategies to obtain relatively large CNCs, pulse laser-induced liquid-solid interface reaction (PLIIR) was used to convert amorphous carbon deposited on Si wafer surfaces, and water-acetone-ethanol as liquid, into CNCs with truncated shape as expected for C8-type structure. The CNCs had a well-defined bandgap, as evidenced by the emitted purple-blue wavelength light in the cathodoluminescence spectrum [11].

Despite many interesting properties of various carbon materials and nanocomposites of nanocube morphology, reported methods for CNC materials require numerous steps and are energy intensive. These include the preparation of the MOF precursor, carbonization, and metal etching. While most of the MOF preparation methods require hazardous organic solvents or are not easily scalable, the metal etching from final carbons leads to large volumes of neutralization waste. Fewer examples of less energy-intensive and template-free methods yielding CNCs without a template have been reported, such natural product (mahua flower) extracts conversion into ~5 nm-sized cubes, which exhibit interesting electronic properties for sensor applications [13]. However, direct methods for obtaining high surface area CNC materials with well-developed internal particle porosity are still missing.

A possible solution to achieve the more straightforward formation of CNCs is to use graphene fragments as the precursor. In this regard, recent computational models suggest that fragments of graphene ribbons fold into nanocubes through inverse Stone-Thrower-Wales (ISTW) defects and in addition to adatoms. The proposed fragment was of single-layer graphene, and so was the resulting CNC [23]. Besides presenting an interesting alternative to the development of novel CNCs, especially high surface area materials with hierarchical pores, experimental demonstration of nanoribbons (NRs) of graphene-type materials converting into CNCs had not yet been realised.

Recently, we reported on a facile method for the preparation of heterogeneous NRs, all having graphene oxide (GO) composition and with large, preserved graphene domains along these ribbon particles [24]. These materials were obtained from the oxidation of carbon black (CB) BP 2000 in aqueous nitric acid ($HNO_3$). Materials had particles with 30 nm in width, and lengths ranging from less than 100 nm and up to several microns. Given the presence of lattice defects in the starting carbon black precursor, and the oxidation of the obtained NRs, such structures provide a favourable platform for the development of carbons having distinct morphologies. In this work, we demonstrate that pyrolysis conditions, namely heating rate, and the starting GO material result in highly porous carbons. Pyrolysis of GO nanoparticles and carbon dots yield microporous carbons with bulk morphologies; however, CNCs are exclusively obtained from NRs at slow heating rates from GO, whereas fast heating rates lead to bulk morphologies, herein labelled bulk porous carbon (BPC). The activated carbon nanospheres, here labelled KPC, were obtained from precipitation of the NR suspensions with KOH solutions. Carbons had surface areas ranging from 500 $m^2/g$ for carbons obtained from different GO and carbon dot particles, all the way up to 776 $m^2/g$ for the CNCs from NR precursor. Only KPC materials had higher surface areas of approximately 2000 $m^2/g$, because of the KOH activation. While many methods exist for the preparation of carbon nanospheres that have attracted considerable interest for $CO_2$ capture [6], the ability to make CNCs with high $CO_2$ to $N_2$ selectivity from such abundant precursor, and without the need for activation, makes this method of interest for scaleup and practical applications. Besides providing an inexpensive and facile method for the preparation of highly porous CNCs, this work provides some experimental support for the folding of ribbon fragments into cube shapes. Given the presence of other carbon fragments, it is expected that the folding takes place with the simultaneous self-assembly of the smaller oxidised fragments, i.e., carbon dots.

## 2. Experimental

### 2.1. Synthesis of NRs

The synthesis of NRs, of GO nanoparticles and carbon dots (CDs) from different grades of CB was reported elsewhere [24]. Briefly, 5 g of CB (Pearl 2000) was placed in a round bottom flask containing 100 mL nitric acid ($HNO_3$) and stirred at 90 °C for 120 h. Then, the mixture was cooled down and centrifuged for 30 min (5000 rpm) followed by discarding the sediment. The supernatant containing carbonaceous nanoparticles (NR, GO, CD) was evaporated under a vacuum yielding light brown powder. Obtained products were used for the next step without any further process and purification.

### 2.2. Synthesis of microporous carbons (CNC and BPC) from NRs

1 g of NR was placed in a ceramic boat in a horizontal cylindrical furnace with an inner diameter of 35 mm and then heated at a rate of either 3 °C/min or 50 °C/min from room temperature and up to 800 °C under flowing Ar atmosphere. Heating was kept for 1 h, then, the furnace was naturally cooled down to room temperature under Ar flow. The resulting black powders were labelled CNCs for the carbon nanocubes obtained at 3 °C/min heating rate. Those obtained at the heating rate of 50 °C/min were labelled BPCs, indicating these are microporous carbons with bulk particle size and undefined morphology at the nanoscale.

### 2.3. Synthesis of aggregated microporous nanospheres from NRs

1 g of NR was transferred to 30 mL of an aqueous KOH solution (0.38 M) and stirred at room temperature for 2 h. Then the water was evaporated, and the obtained reddish solid was placed in a ceramic boat in a horizontal cylindrical furnace with an inner diameter of 35 mm. The furnace was heated at a rate of 3 °C/min up to 800 °C under Ar and kept at this temperature for 1 h. The furnace was finally allowed to cool naturally down to room temperature under Ar flow. The resulting black powder was washed thoroughly with water and a solution of HCl (0.1 M) several times until a pH ~6.5–7.0 for the water rinse was reached. The black powder was dried at 80 °C for 8 h and labelled KPC.

### 2.4. Characterization

$N_2$ isotherms at 77 K were measured using a Micromeritics ASAP 2020 Plus volumetric analyser (Micromeritics Corp, Norcross, GA, USA), and the Quantachrome Nova 2000E (Quantachrome Instruments, Boynton Beach, FL, USA). Prior to adsorption measurements, all samples were degassed under vacuum and at 200 °C for at least 4 h. Specific surface areas were calculated using the Brunauer–Emmett–Teller (BET) method within the relative pressure range selected using Rouquerol recommendation [25,26]. The total pore volumes were taken directly from the adsorption isotherms at the relative pressure of 0.98, except for a few indicated samples. Pore size distributions (PSD) for $N_2$ were calculated using non-local density functional theory (NLDFT) assuming carbons with slit-pore geometry and the equilibrium model. The $CO_2$ isotherms were measured at 273 K for all samples in a Quantachrome Nova 2000E (Quantachrome Instruments, Boynton Beach, FL, USA). Measured pressures were normalised by the vapor pressure of $CO_2$ at this temperature, i.e., 26,236 mmHg. The $CO_2$ PSD curves were calculated using NLDFT for slit-pore geometry and Monte Carlo methods for comparison.

Scanning transmission electron microscopy (STEM) and high-resolution transmission electron microscopy (HRTEM) imaging of the materials was performed using a Thermo Scientific Talos F200X Transmission Electron Microscope. The materials were dispersed on a holey carbon-coated copper grid. Selected area electron diffraction (SAED) patterns were obtained in TEM mode with a 200 keV electron beam without sample tilt. Energy-dispersive X-ray spectroscopy (EDS) was conducted to obtain chemical information. Scanning electron microscopy (SEM) images of the materials were obtained with a JEOL 7800F FEG SEM (JEOL, Akishima, Tokyo, Japan).

X-ray photoelectron spectroscopy (XPS) analysis was performed using the Thermo K-Alpha instrument (Thermo Fisher Scientific). Prior to measurements, the samples were placed onto the Cu grid substrate and outgassed under vacuum and room temperature for 5 days. The pass energy for the C1s line was 0.05 eV and 0.1 eV for the N1s and O1s lines. For each sample, 10 spectra were collected for the C1s and O1s, and 20 spectra were collected for N1s narrow profile. Selected areas of these samples were etched with the X-ray gun for 20 s and the spectra were collected for verification of the consistency of the quantitative analysis. The neutralising Ar-ion gun was used for the entirety of each measurement. Spectral fittings for the latter were performed using the Avantage software package. Peak fitting of the narrow region spectra was performed using a Shirley type background, and the synthetic peaks were calculated by the Powell method for a Gaussian-Lorentzian mixed sum.

The Raman data of the carbons were recorded at room temperature using a Renishaw inVia Raman Microscope (Renishaw plc, Miskin, Pontyclun, UK) with an excitation wavelength of 457, 514, and 633 nm. The Raman mapping was recorded at room temperature using a Renishaw Raman QONTOR with an excitation wavelength of 488 nm, and 2400 $mm^{-1}$ grating. The exposure time was 0.100 s for 1 accumulation. The spectral range was 743 $cm^{-1}$ to 2177 $cm^{-1}$. This was a StreamHR image measurement created by the StreamHR image acquisition wizard.

The elemental analyser (Vario EL Cube, Germany) was used to determine the amounts of carbon, nitrogen, and oxygen. Thermogravimetric analysis (TGA) was carried out using a 10 mg sample placed in an alumina pan with a TA Instruments SDT Q600 at different heating rates from the room.

### 2.5. $CO_2$ adsorption set-up

Quantachrome iSorb High-Pressure Gas Analyser (Germany) was used for $CO_2$ adsorption and selectivity of $CO_2$ over $N_2$ studies. All the sorbents were degassed at 160 °C under vacuum for 2 h prior to the adsorption study. $CO_2$ adsorption performance of carbons was measured volumetrically in an iSorb apparatus at four different temperatures (0, 25, 35 and 45 °C) and pressures from 0.1 to 10 bar. The degasification temperature was internally controlled by covering the cell-containing sample with a thermal jacket, while the adsorption temperature was adjusted by a jacketed beaker connected to a circulating bath containing water and ethylene glycol. For each experiment, about 200 mg of any carbon sample was used for the adsorption studies. $CO_2$ (99.9%) and $N_2$ (oxygen-free) as gas sources were used throughout the experiments. $N_2$ adsorption experiments at 25 °C and different pressures were also recorded through the same procedure for $CO_2$. The laboratory-scale set-up employed to conduct $CO_2$-adsorption experiments is illustrated in Fig. S1.

## 3. Results and discussion

In our recent work, the oxidation of different CB precursor materials in $HNO_3$ was investigated [24], and results agreed with previous reports for materials including acetylene black, Monarch and Vulcan [27,28]. Extended oxidation times of these materials yielded oxidised forms of carbon dots or GO nanoparticles, depending on the starting CB. Both, the products, and the yield varied with the amount of amorphous carbon and surface area of the precursor. For CBs, the greater the content of amorphous carbon, the lower the surface area. Lower yields of graphene nanomaterials are consequently obtained as greater fractions of the CB particles contain more crosslinked disordered carbon and fewer graphene fragments in the basic structural units (BSUs). For the low surface area acetylene black, carbon dots form in small amounts, with most of

the product being an oxidised CB precipitate. The oxidation of BP 2000, with a very high surface area of 1700 $m^2/g$, however, resulted in large yields of GO NRs, as presented in Fig. 1.

The NRs were all roughly 30 nm in width, with the length varying from a few tens of nanometres to several micrometres. The high surface area, resulting from the deep micropores formed between stacks of the graphene-type fragments forming the basic structural units (BSUs) of CB, allowed for the enhanced accessibility of $HNO_3$ to these domains. The accessibility to these domains favoured the oxidation reaction and increased the yield of the product separated during the synthesis. The obtained NR products further resemble the fragments forming the BSUs of BP 2000 and the interconnecting carbon film binding the discrete CB spheres forming the primary aggregate structure [24,29].

The optical image of an NR sample drop-casted on a glass microscope slide was taken using the microscope stage in the Raman instrument (Fig. 2). This image shows the large number of ribbons present, and with lengths exceeding tens of microns in some particles, and with multiple smaller fragments with more rectangular and square shapes. Some larger fragments with random shapes are also seen. Raman maps for the D and G bands of the selected region indicated in the optical image, which includes the small NR fragment confirm the previous findings that these ribbons have a heterogeneous structure along the basal plane.

Graphene has been proposed as the building block of various graphitic carbon nanomaterials, including single and multiwalled carbon nanotubes, fullerenes, and graphite [30]. The stacking, folding or rolling of appropriate graphene fragments could theoretically lead to all the different carbon allotropes with C $sp^2$ hybridization. Recent computational studies on graphene fragments support the folding of graphene fragments into cubes using both ISWT defects and adatoms

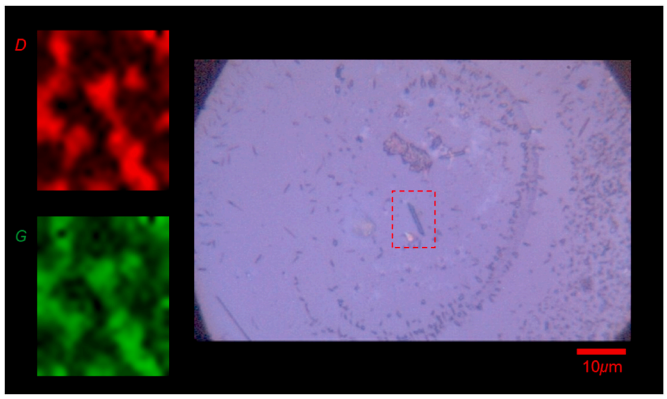


**Fig. 2.** Optical image of nanoribbons (centre) and highlighted region (dashed red rectangle) used for generating the blown-out Raman maps for the *D* and *G* bands. (A colour version of this figure can be viewed online.)

[23]. ISTW defects are comprised of heptagonal carbon rings connected by a pentagonal ring [31]. The Stone-Thrower-Wales (STW) defects are similar, but with two pentagonal rings connected by a heptagonal ring [32]. Both STW and ISTW are known to provide curvature to graphene fragments. Such defects have also been proposed to exist in carbon blacks [33], and lines of alternating pentagonal and heptagonal C rings have been directly visualized by aberration-corrected high-resolution transmission electron microscopy (HR-TEM) on graphitizing microporous carbons [34]. Hence, existing lattice defects in the BSUs of the starting CB would be transferred to the derived fragment. Besides the

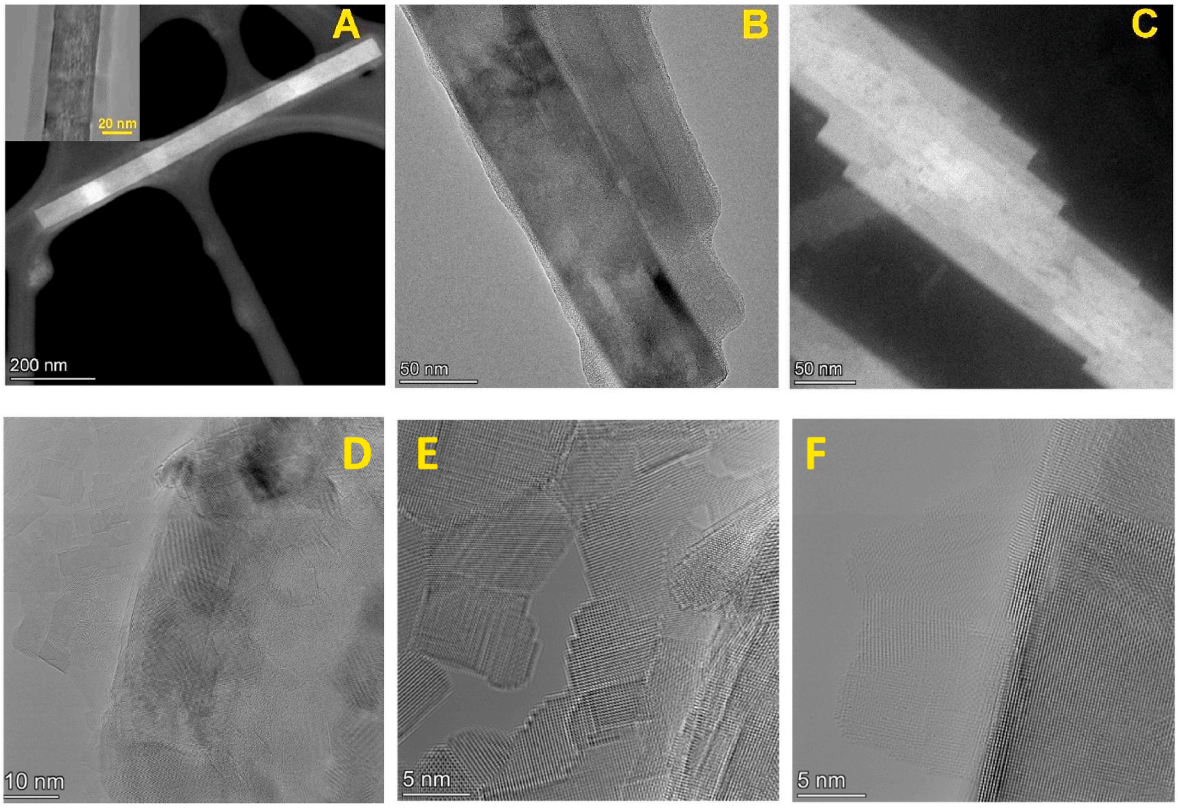


**Fig. 1.** STEM and TEM images of nanoribbons used as precursors for the different reported porous carbon materials, including carbon nanocubes. Low magnification STEM image and high-resolution TEM image inset (A) of nanoribbons made from the oxidation of more ordered BP 2000 shows a width of ~30 nm and length varying from a few tens of nanometres to several micrometres. High magnification TEM and STEM images in (B) and (C) show the nanoribbon fragments with different lengths and aggregated layers. In panel (B), carbon from the TEM grid is also observed. Aberration corrected high-resolution TEM images (D, E and F) of selected regions of the NR samples. These confirm that NRs are formed of multi-stacked graphene fragments and with some monolayer regions (F). (A colour version of this figure can be viewed online.)

potential transfer of ISTW defects, additional oxygen, and nitrogen groups in the basal planes of the NRs contribute to the additional breaking of the C–C bonds and consequent formation of vacancies resembling STW and ISTW defects. Added to the insertion of these heteroatoms within the basal planes in ring structures, both defects contribute to the breaking of the hexagonal arrangement of C atoms in the graphene sublattice of these NRs. The O and N atoms sitting in positions above or below these graphene planes may further act as adatoms. Such groups may also contribute to the structural folding of NRs into cubes, and similarly as C adatoms in graphene ribbon fragments [23]. Because of the multilayer structure of the present GO nanoribbons, and the presence of O and N groups that provide dipole and H-bonding interactions, van der Waals forces maintain individual graphene layers and fragments together during thermal treatments. It has also been observed in STEM analysis, that fragments of NRs that are smaller than 100 nm tend to stack on the surfaces of the micron size NRs. The assembly of these smaller fragments, in addition to existing CD particles, and of larger GO fragments with the NRs having different lengths must be considered. As a result of this complex assembly and folding of 2D fragments, a multi-shell carbon cube structure forms. During the thermal treatment, shrinkage and densification of the carbon walls should also be considered. This shrinkage may take place along preferential directions given the planarity of the starting building blocks.

During the thermal treatment, the NR individual sheets crosslinked and micropores formed. The possible explanation for the porosity development during crosslinking is the evolution of $H_2O$ during condensation of hydroxyl groups and from the decomposition of carbonyl/carboxyl edge and basal plane sites. This was previously observed in our studies on the preparation of microporous carbon spheres obtained from benzene polycarboxylic acid precursors [35,36]. Slow heating rates possibly allowed the NR building blocks to overcome H-bonding interactions between adjacent NR domains, thus leading to monodisperse CNCs. Under fast heating rate conditions, these adjacent graphene fragments are laterally crosslinked prior to folding into cubes, thus yielding carbons with bulk morphology. Micropores formed from similar evolution of gases from condensation reactions and fragmentation of O and N functionalities.

STEM images of CNCs (Fig. 3) confirmed the cube morphology of the obtained carbons from slow pyrolysis of NRs. These are uniform in size throughout the analysed samples on the TEM grids and have approximate widths of 250 nm. The low magnification STEM image in Fig. 3C shows individual and small agglomerates of the CNCs. The unit particles forming the agglomerates are also CNCs of approximately the same size. High magnification STEM of an agglomerate of CNCs in Fig. 3D shows that it is still possible to discern the cube morphology of the individual particles. The STEM image in Fig. 3E highlights that the edges of the NCs are slightly rounded and that the additional fringes confirm the presence of micropores, without any long-range atomic periodicity. The calculated $d_{002}$-spacing for the NR precursors was >0.35 nm, which is characteristic of turbostratic carbons. Despite the existence of large graphene domains along these NRs, many structural defects and heteroatoms in the basal and edge sites, combined with interparticle crosslinking, prevent the individual sheets from having the Bernal stacking expected for graphite. The same is expected for the crosslinking and assembly of the GO and CD fragments during this process [33].

The resulting CNC and BPC materials were essentially amorphous and no lattice fringes for two-dimensional periodicity were seen in the Fast Fourier Transform (FFT) pattern in Fig. 3F. The Raman spectra of these carbons, in Fig. S2, further confirmed the turbostratic nature of the materials with the pronounced D and G bands that were both broad and had comparable intensities, regardless of particle morphology. Interestingly, the CNC powder was composed of micron-sized particles without any discernible features, as seen in the FE-SEM image presented in Fig. S2. Only after sonication, the cube-shaped nanoparticles could be visualized in the STEM. The TEM images for BPC samples are shown in Fig. S3.

The assembly of these NRs, GO fragments and CDs is further demonstrated by the precipitation of nanospheres in a KOH solution. The KOH co-precipitated with NR, GO and CDs. After carbonization, the nanospheres formed linked agglomerates, rather than being monodisperse as verified by (S)TEM images in Fig. 4 and Fig. S3. Micropores are also formed by evolved gases, with some minor contribution of KOH activation [37].

The primary element lost during the pyrolysis was N, as evidenced by the sharp decrease in the composition of this element in comparison with NR and BPC samples. The N content was as low as 0.26 wt% and 0.28 wt% in the elemental and XPS analyses results, respectively (see Table S1). Despite the low concentration of KOH in the solution used to precipitate the NRs, the surface area values exceeded those for CNC and

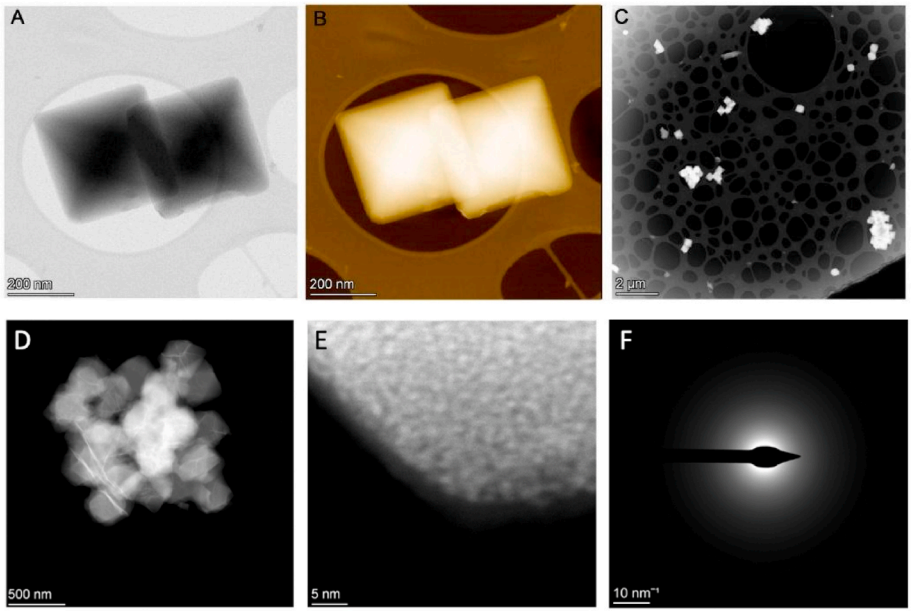


**Fig. 3.** STEM images of CNCs shown in bright-field (A) and high-angle annular dark-field (HAADF) (B). C, D and E show the CNCs from low to high magnifications. The selected area electron diffraction pattern of CNCs (F) indicates the amorphous feature of these CNCs. (A colour version of this figure can be viewed online.)

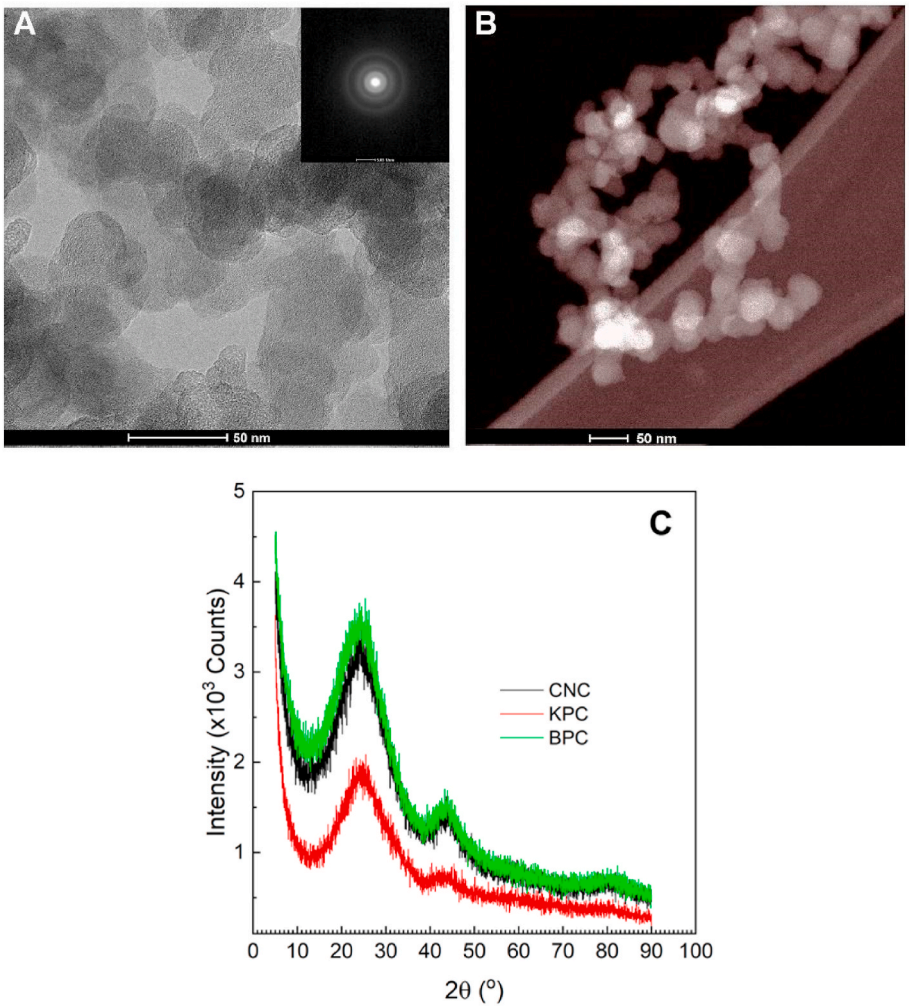


**Fig. 4.** TEM image (A) and HAADF-STEM image (B) of KPC indicate that the nanospheres formed linked agglomerates rather than being monodisperse after carbonization. The selected area electron diffraction pattern (inset in A) shows the amorphous nature of this porous carbon. XRD patterns for the synthesized porous carbons (C). (A colour version of this figure can be viewed online.)

BPC materials. As for CNC and BPC particles, these KPC aggregates of spherical particles also lack the long-range atomic periodicity of graphitic carbons despite the two-dimensional stacking of carbon planes. This is evidenced by the HRTEM in Fig. S3C.

The XRD patterns for all samples (CNC, BPC, and KPC) presented in Fig. 4C also suggest the amorphous carbon structures. These patterns have broad peaks that result from largely destructive interference of diffracted X-rays and in the regions where the diffraction peaks for graphite are expected. The first diffraction peak for graphite originates from the 3D periodic stacking of the graphene planes with ABAB … stacking sequence. This corresponds to the (002) diffraction plane of graphite at $2\theta \sim 26.5^{\circ}$. Stacking defects, increase in interplanar spacing, and lack of periodicity result in peak shifts to smaller angles, peak broadening and loss of intensity. Additionally, the lack of coherently planar and abundance of curved graphene layers, in-plane defects (broken bonds, missing atoms, heteroatoms), and the short range of stacked domains induced by basal plane defects and crosslinking between stacked domains lead to the same effects for the subsequent (100) and (110) diffraction peaks in the expected XRD pattern of graphite. Hence, only two broad and low intensity peaks are seen for turbostratic carbons. As in the case of turbostratic graphene-based materials, porous carbons have large heteroatom contents, such as oxygen, and additional crosslinking between short graphene domains that takes place during the pyrolysis process, both of which leads to extensive structural disorder [33,38].

As seen in the starting NRs, the CNCs and BPCs also contained large amounts of oxygen and nitrogen, which were found to be uniformly distributed throughout the samples. The EDS mappings of a small CNC agglomerate are presented in Fig. 5 and Fig. S4. Moreover, the XPS spectra for the CNCs and bulk carbons are given in Fig. 6 and Fig. S5, respectively. A summary of the elemental composition of these materials from EDS and XPS is given in Table S1. Differences are expected, as the former includes C and O from the grids used to support the samples for STEM. Interestingly, the distribution of oxygen groups differs from the surface to the bulk of the particles in these carbons. Compared to the NRs, for which the initial oxygen concentration was ~50 wt% from the EDS, that of the CNCs was considerably less, ~12 wt%. This corroborates with the proposed mechanism for the formation of micropores from the elimination and/or decomposition of oxygen functional groups during the thermal treatments. The bulk carbon particles obtained had nearly 23 wt% oxygen, indicating that particle growth proceeded mostly from the condensation and elimination of oxygenated groups along the NR edges and outermost surfaces of the ribbons. The thermal decomposition profiles were similar for these NRs at various heating rates investigated during thermogravimetric analysis (TG), namely 3, 20, 40 and 60 °C/min. As seen in Fig. S5, the carbon yield is approximately 20–23 wt% at 800 °C under flowing Ar. Approximately 10 wt% weight loss around 100 °C corresponds to physically adsorbed water in the starting NRs. Additional weight loss in the ranges near 200 °C possibly results from the condensation reactions during crosslinking. At higher

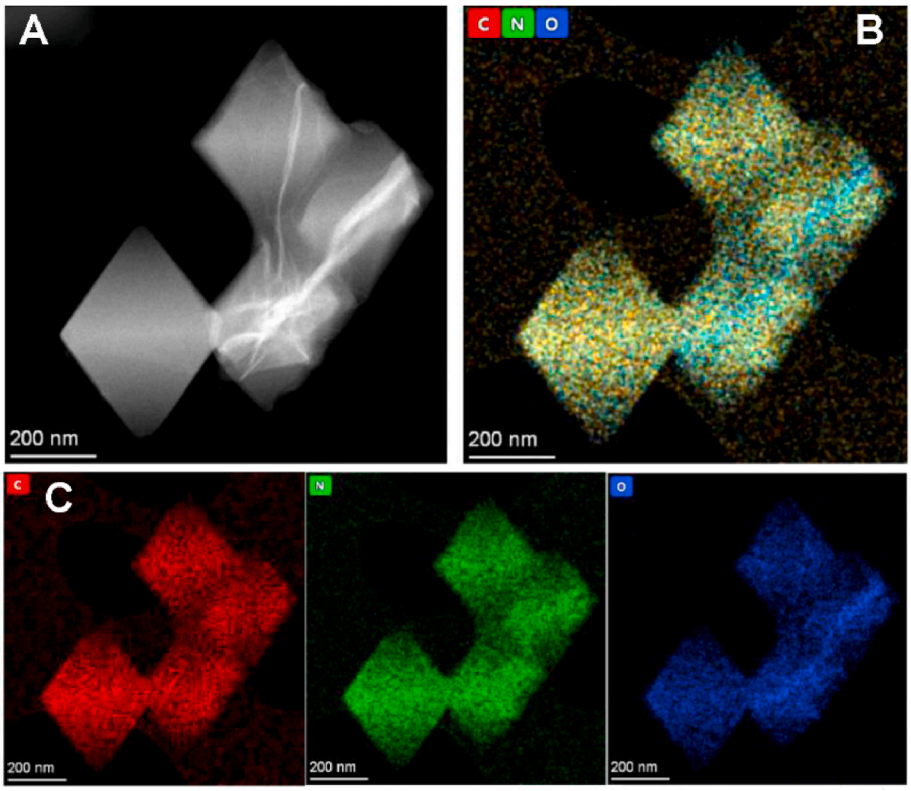


**Fig. 5.** HAADF-STEM image of carbon nanocubes (A) and composite EDS map of C, N and O for the same imaged particles (B). Corresponding individual EDS maps for C, N and O (C). The background EDS signal contributions from the TEM grid also appear in the image maps. (A colour version of this figure can be viewed online.)

temperatures, GO materials lose most of their oxygen content, and some of the carbon to which oxygen was bonded to, during thermal treatments.

X-ray photoelectron spectroscopy (XPS) was used to further investigate the functional groups present on the surface of the porous carbons, see Fig. 6 and Fig. S6. The commonly used adventitious carbon C–C/C–H peak of 284.5 eV (sometimes 284.8 eV) [39,40], was not used for charge reference. This correction has been the subject of recent debate given that the contributions to spectral shifting go beyond that of electrostatic charging. Hence, such correction may be unreliable for full spectral correction, and more complex correction requires the inclusion of the work function of the material [41].

The carbon spectrum for all species was asymmetric which is characteristic for materials with dominant C–C ($sp^3/sp^2$) components. CNC contained oxygenated carbon species, which were predominantly carbonyl functional groups; however, carboxylic groups may also be present in BPC. As corroborated by elemental analysis, nitrogen was present in small quantities in CNC. In the carbon 1s spectrum, the signal corresponding to the C–N bond overlapped with the C–OH and C–O–C signals, meaning that it was not possible to obtain a specific peak location corresponding to C–N. However, in the N 1s spectrum, despite the small quantity of nitrogen present giving slightly noisy spectra, it was possible to pick out the main peaks and assign them accurately following literature precedent. CNC contained more pyrrole/pyridone nitrogen than pyridine-type nitrogen. The oxygen spectra are dominated by the carboxylic peak. A summary of the XPS synthetic peaks is given in Tables S2–S4 in **SI**.

The adsorption properties were calculated from $N_2$ at 77 K and $CO_2$ at 273 K. The adsorption isotherms and the corresponding pore size distributions (PSDs) are presented in Fig. 7, and the calculated results are summarized in Table S4. The $N_2$ isotherms for the CNC and BPC materials were type I, which is characteristic of microporous carbons. The isotherms for BP 2000 and KPC are presented as the inset in Fig. 7A. The adsorption isotherm for the BP 2000 was a combination of types I and II, with high gas uptake at low relative pressure, and an infinite multilayer formation at high relative pressures. These indicate that the pristine CB has internal primary particle micropores, and macropores formed between particle aggregates, respectively. The hysteresis loop is H3, also expected to be macroporous materials. The KPC sample has a type IV isotherm, characteristic of mesoporous materials. These mesopores form between particles that aggregate and have constrictions. The latter is verified by the H2 hysteresis loop in the isotherm. The pore constrictions are further evidenced by the additional step on the hysteresis loop before closing at the relative pressure of ~0.4. The condensation step occurs at relative pressures above 0.8 because of the interparticle mesopores [26]. This agrees with the calculated mesopore widths between 8 and 10 nm. Most pores, however, are the pore constrictions smaller than 4 nm and internal particle micropores (<2 nm). These are evidenced by the calculated PSD, which is comparable to that of the starting BP 2000 (Fig. 7B). The latter, however, has very large mesopores and small macropores (not shown). The PSDs for CNCs and BPC have few micropores with widths between 1 and 2 nm.

To assess smaller micropores, low pressure $CO_2$ adsorption isotherms were measured at 273 K (Fig. 7C) and were used to calculate the PSDs for pores with widths up to 1.5 nm. The results do show that while some micropores are about 0.8 nm in width, the distribution curves for most pores are centred around 0.6 nm. These small micropores are further classified as ultramicropores. KPC has a broader distribution near 0.5 nm, and it has a higher volume of pores larger than 0.8 nm. The calculated PSD for KPC indicates a larger fraction of pores is in the ultramicropore range. Whereas those for BP 2000 are in the supermicropore range (see inset in Fig. 7D). Compared to CNC and BPC, the KPC material has a higher fraction of supermicropores than the former two. Moreover, good agreement is found between the PSD curves calculated from the $CO_2$ isotherms by the NLDFT with those computed using the Monte Carlo method (see Fig. S7).

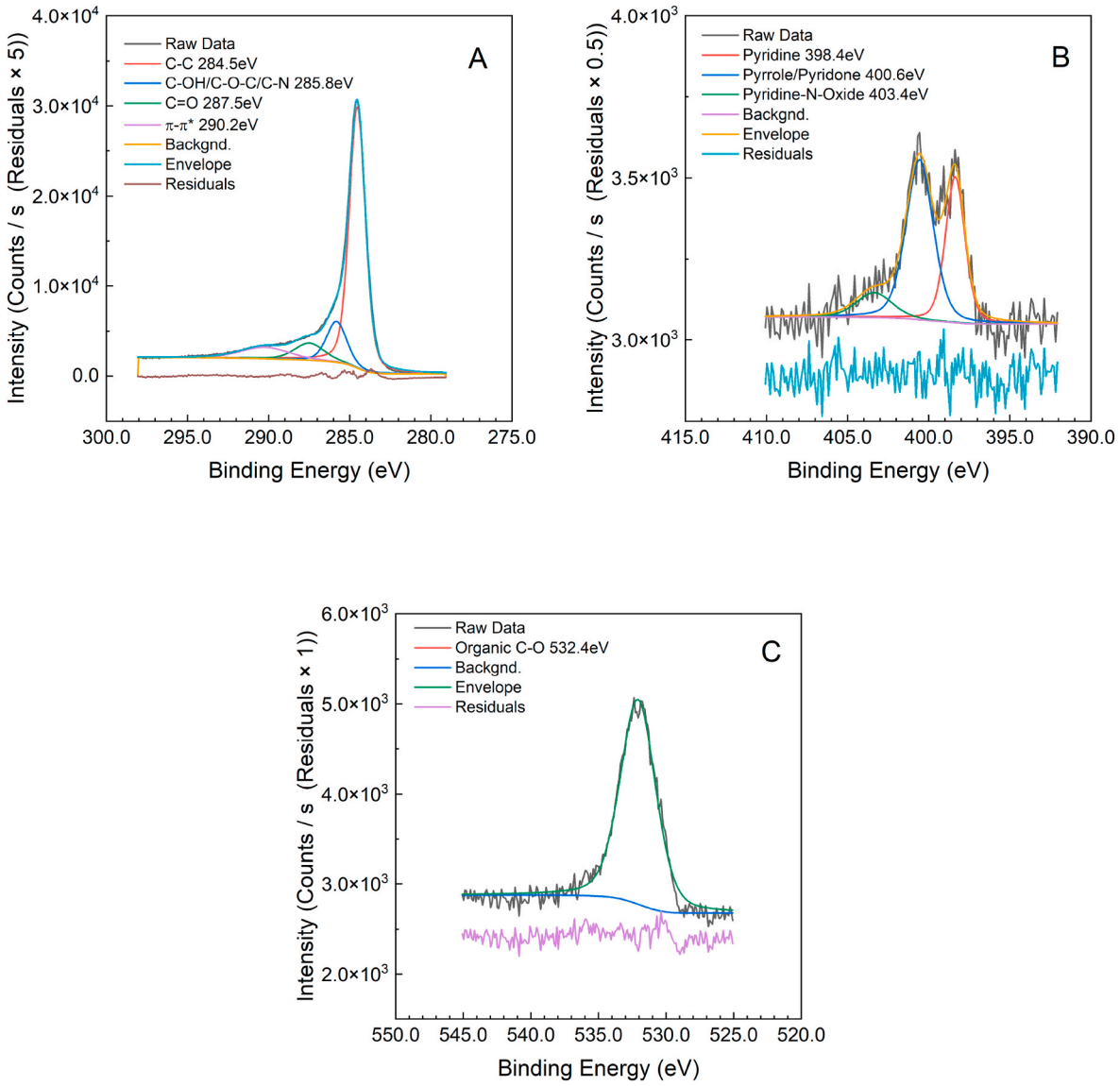


**Fig. 6.** XPS spectra of the C 1s (A), N 1s (B) and O 1s (C) regions of carbon nanocube materials. The residuals have been vertically offset by different amounts in Counts/s for clarity. (A colour version of this figure can be viewed online.)

Porous carbon materials with controlled adsorption properties are of interest for renewable energy applications [42,43], particularly gas capture [1,2,44,45]. For $CO_2$ separation from post-combustion effluents at ambient pressures, the adsorption capacity and the selectivity over other gases, mostly $N_2$, are important parameters [46]. The $CO_2$ isotherms at 298 K for all the porous carbons synthesized is presented in Fig. 8.

Below ambient pressure, the $CO_2$ adsorption capacity for CNCs exceeded that of the BPC and KPC materials, reaching 3.7 mmol/g at 1 bar of pressure. The small differences between CNC and BPC may originate from the higher specific surface area of the former as compared to the latter (>100 $m^2$/g). The higher $CO_2$ uptake below 1 bar for CNC and BPC compared to KPC may result from the higher ratio of ultramicropores to supermicropores found in CNCs and BCPs [47,48]. At 10 bar, KPC adsorption far exceeded that of the other two carbons, reaching 12 mmol/g versus the 6.4 mmol/g for CNCs. The higher total amount of $CO_2$ uptake for KPC resulted from the higher total micropore volume and the additional mesopores found in this material [49,50].

We note that all materials have very low $N_2$ uptake under the same conditions as applied for $CO_2$ uptake. For CNCs, the $CO_2$ uptake is nearly 23 times that for $N_2$, whereas for BPC, this drops to 13 times, both at 1 bar. The selectivity for the adsorption of a binary mixture of these gases can be predicted from the single component isotherms by the Ideal Adsorbed Solution Theory (IAST). This theory assumes similar interactions between different gas molecules in a mixture, here $N_2$ and $CO_2$, with the sorbent surfaces [51]. Recent studies indicate that for carbon materials with a high volume fraction of ultramicropores, the N-doping did not influence the $CO_2$ uptake as compared to undoped carbons [47]. Hence, IAST is applicable to predicting the adsorption of binary $CO_2/N_2$ mixtures for a series of samples having similar surface chemical composition and porosity. The selectivity ($S_{ads}$) is estimated according to Eq. 1, where $q_i$ and $p_i$ are the molar uptake and the partial pressure of the species $i$, respectively, and the ratio $\frac{q_i}{p_i}$ yields a value that is analogous to the equilibrium constant obtained from Raoult's law for the solubility of gases in liquids.

$$S_{ads} = \frac{\left(\frac{q_1}{p_1}\right)}{\left(\frac{q_2}{p_2}\right)}$$

In the case of KPC, for a total pressure of 1 bar and an expected 0.15 bar

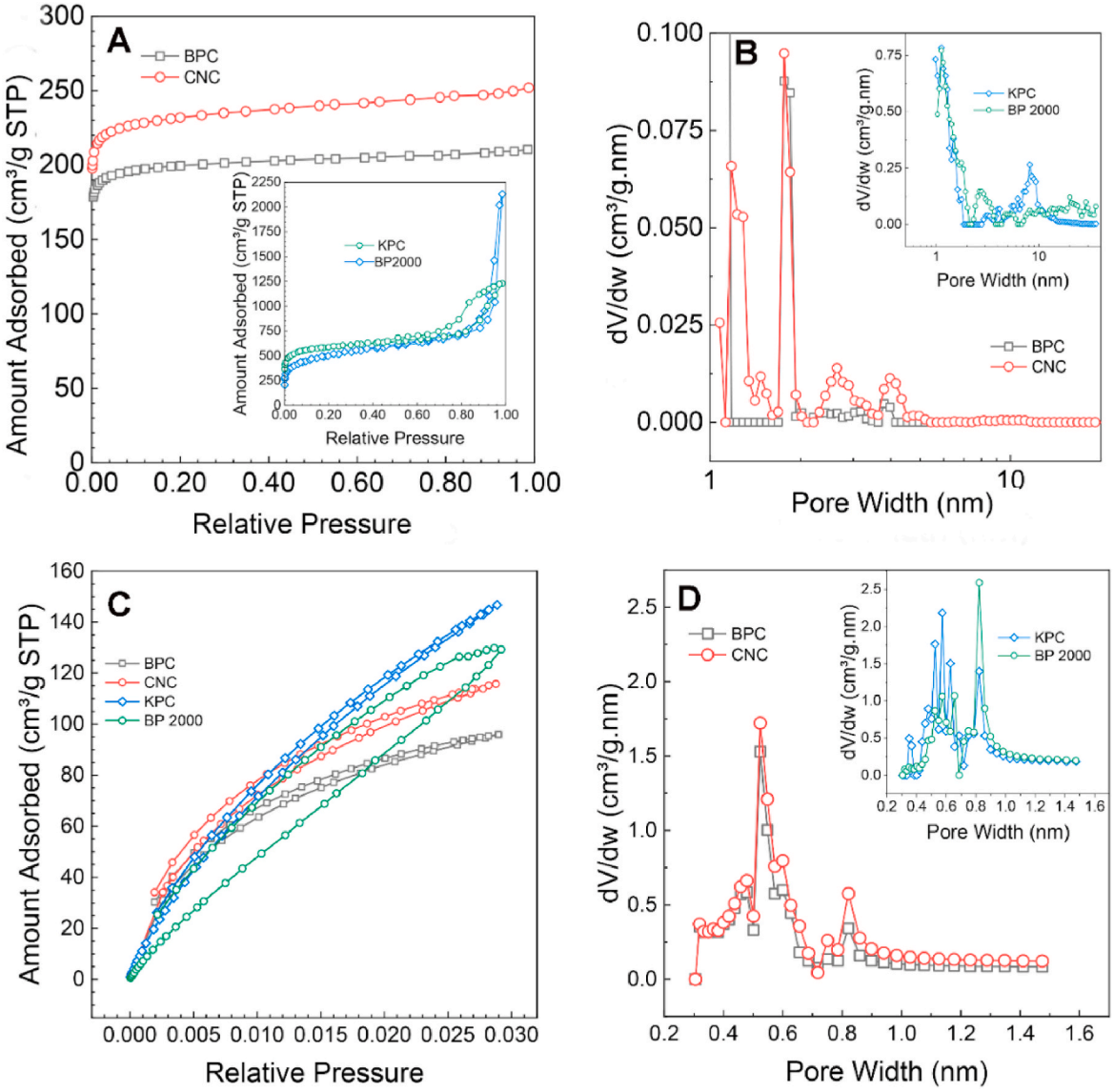


**Fig. 7.** (A) $N_2$ at 77 K isotherms and (B) corresponding NLDFT pore size distributions; (C) $CO_2$ at 273 K isotherms and (D) corresponding NLDFT PSD curves. (A colour version of this figure can be viewed online.)

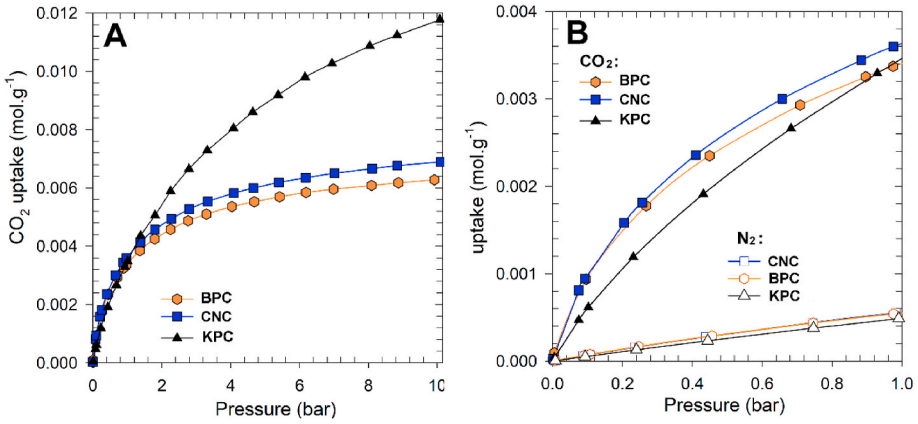


**Fig. 8.** $CO_2$ adsorption isotherms measured at 298 K (A) and low-pressure isotherms versus $N_2$ isotherms measured at the same temperature (B). (A colour version of this figure can be viewed online.)

$CO_2$: 0.85 bar $N_2$ in a post-combustion gas mixture, the experimental uptake for $CO_2$ at 0.15 bar is 0.9 mmol/g and for $N_2$ at 0.85 bar is ~0.41 mmol/g. The predicted selectivity for KPC (~0.9 mmol/g $CO_2$ and ~0.41 mmol/g $N_2$) dropped to ~13. Previous studies on microporous-mesoporous carbons pointed to the importance of ultramicropores and N-doping for high $CO_2$ uptake and selectivity [47–50,52,53]. In the present study, the relevance of N-doping for $CO_2$ is clear, as CNC has the highest N content, and yet the comparable volume of ultramicropores to both BPC and KPC materials. Similar conclusions on the importance of pore size and micropore volume for the selective adsorption of $CO_2$ have also been verified for N-rich materials, such as boron nitride [54]. In general, the $CO_2$ uptake and selectivity for KPC and CNC were in range with those for microporous carbons having spherical morphology and obtained by a modified CVD method [35]. Comparison to additional selected reported materials is provided in Table 1. Data on biomass derived carbons can be found in comprehensive reviews elsewhere [44,45,52].

Although adsorption capacity is comparable to most published for different activated carbons, the present CNCs offer many advantages. First, the abundance and low cost of the starting NR precursor, namely BP2000. Second, the simplicity of the method allows for the scalability of the NRs for subsequent uses. For instance, this process eliminates the need for activation, and it leads to a metal-free single neutralization stream from the starting NR preparation. Furthermore, in this new method, a single thermal treatment is required for preparing highly microporous CNCs. Third, the fact that these CNC particles are largely monodisperse or found in small aggregates. The bulk of the surface area results from the internal particle porosity. The result is particles having a high surface-to-volume ratio, which favours gas accessibility to the storage sites. In this respect, cubic shaped nanoparticles have a greater surface-to-volume ratio than spheres of comparable dimensions. Moreover, cubic structures lead to better charge transfer between particles than spherical ones. This has been found for semiconducting quantum dots, where the flat faces of two dots lay flat against each other, thus creating a stronger coupling between the quantum dots [65]. Another important aspect of cubic structures with rounded edges, as in the present CNCs, is that they have been found to self-assemble into a larger variety of superstructures as compared to cubes with sharp edges and spheres. In a study simulating superstructures of different inorganic nanoparticles, those particles having rounded cube edges could assemble into numerous icosahedral superstructures [66]. Such studies indicate a higher degree of anisotropy in superstructures and agglomerates as compared to sharp-edge cubes, and to spherical particles [66]. As most often reported to monodisperse spherical carbon particles, these structural properties of CNCs are particularly interesting for assembling composites with films, membranes, and monoliths, or as for uses in separations [6], catalysis [4,67], and energy storage and conversion devices [6,68].

**Table 1**
Comparison of recently reported porous carbon materials for $CO_2$ capture at 1 bar and 25 °C.

| Sorbent type | Precursors | Activation agent | $CO_2$ Uptake (mmol. $g^{-1}$) | Ref. |
|---|---|---|---|---|
| Carbon Sphere | Pyromellitic acid | None | 2.90 | [35] |
| Holey graphene frameworks | Graphene oxide | $HNO_3$ | 2.11 | [55] |
| HPCs | Polyphosphazene microspheres | $K_2CO_3$, KOH, and NaOH | 4.28 | [56] |
| N-doped porous carbon | Waste Wool | KOH | 2.91 | [57] |
| N-doped porous carbon | Algae | KOH | 2.76 | [58] |
| Porous carbons | Lotus stalk | KOH | 3.68 | [59] |
| N-doped porous carbon from hydrothermal carbonization | Corn stalk | KOH | 3.97 | [60] |
| Heteroatom-doped porous carbon | Sulphur-containing waste liquid (SCWL) | $K_2C_2O_4$ | 3.82 | [61] |
| N-doped porous carbon | Water lettuce | KOH | 3.48 | [62] |
| Oxygen functionalized porous activated biocarbon | Grape marc | KOH | 3.9 | [63] |
| Hierarchically porous carbons | Glucosamine hydrochloride | $CH_3COOK$, $KHCO_3$, $K_2CO_3$, $K_2C2O_4$ | 2.75–3.35 | [64] |
| CNC | | None | 3.7 | This work |

## 4. Conclusion

We have presented a novel, facile and inexpensive production route to porous CNCs with a high abundance of micropores without needing template or alkali-metal activators. We also showed the pathways in which nanoribbons are architected to yield in a series of porous carbons with different morphology, chemical composition, textural properties, and $CO_2$ capture performance. Some parameters (e.g., heating rate and alkali-metal templating) were investigated to understand their possible effect on the properties of the resulting. The results demonstrated that CNCs only form in the case of slow pyrolysis of nanoribbons while the fast pyrolysis leads to microporous carbons having undefined bulk morphology and with slightly lower surface area and pore volumes than CNCs. Moreover, CNCs can uptake 3.7 mmol/g $CO_2$ at atmospheric pressure and 25 °C while the efficiency decreases slightly in the case of BPCs. Interestingly, pyrolysis of NRs precipitated with KOH yielded carbons with interconnected quasi-spherical nanoparticles. Each individual KPC nanoparticle was ~30 nm in size with internal particle micropores and textural mesopores, both making KPCs suitable for high-pressure $CO_2$ capture. The different nanostructures obtained by different processing methods indicate that CD particle assembly and folding of 2D structures, namely NRs and GO, play a role in the formation of precipitated KPCs, and of CNCs. More comprehensive mechanistic studies on the conversion of NRs into CNCs and KPCs, as well as their potential use for energy separations, catalysis and energy storage and conversion, are ongoing.

## CRediT authorship contribution statement

**Saeed Khodabakhshi:** Conceptualization, Data curation, Formal analysis, Funding acquisition, Investigation, Methodology, Project administration, Resources, Software, Writing – original draft, Writing – review & editing. **Pasquale F. Fulvio:** Conceptualization, Investigation, formal analysis, Writing – review & editing, software. **Krista S. Walton:** Formal analysis. **Sajad Kiani:** Investigation. **Yubiao Niu:** Formal analysis, Investigation. **Richard E. Palmer:** Writing – review & editing. **Andrew R. Barron:** Supervision. **Enrico Andreoli:** Conceptualization, Formal analysis, Investigation, Supervision.

## Declaration of competing interest

The authors declare that they have no known competing financial interests or personal relationships that could have appeared to influence the work reported in this paper.

## Acknowledgement

S. K. wishes to acknowledge funding from the European Union's Horizon 2020 research and innovation programme under the Marie Skłodowska-Curie grant agreement No 663830. Financial support was

also provided by the Reduce Industrial Carbon Emissions (RICE) research operation part-funded by the EU's European Regional Development Fund through the Welsh Government. The authors would also like to acknowledge the assistance provided by the Swansea University AIM Facility, which was funded in part by the EPSRC (EP/M028267/1), the European Regional Development Fund through the Welsh Government (80708) and the Sêr Solar project via the Welsh Government. Use of the TAMU Materials Characterization Facility for AFM and HRTEM, and Dr. Winson C. H. Kuo are acknowledged. Use of the GT IEN/IMAT Materials Characterization Facility for XPS and Raman Mapping is acknowledged.

## Appendix A. Supplementary data

Supplementary data to this article can be found online at https://doi.org/10.1016/j.carbon.2024.118940.

## References

[1] J. Jjagwe, -.P.W. Olupot, -.E. Menya, -.H.M. Kalibbala, Synthesis and application of granular activated carbon from biomass waste materials for water treatment: a review, J. Bioresour. Bioprod. 6 (4) (2021), 292.
[2] B.A. Goodman, Utilization of waste straw and husks from rice production: a review, J. Bioresour. Bioprod. 5 (- 3) (2020) 145.
[3] C. Portet, G. Yushin, Y. Gogotsi, Effect of carbon particle size on electrochemical performance of EDLC, J. Electrochem. Soc. 155 (7) (2008) A531.
[4] V. Yarlagadda, M.K. Carpenter, T.E. Moylan, R.S. Kukreja, R. Koestner, W. Gu, L. Thompson, A. Kongkanand, Boosting fuel cell performance with accessible carbon mesopores, ACS Energy Lett. 3 (3) (2018) 618–621.
[5] R. Leyva-Ramos, C. Geankoplis, Diffusion in liquid-filled pores of activated carbon. I. Pore volume diffusion, Can. J. Chem. Eng. 72 (2) (1994) 262–271.
[6] J. Liu, N.P. Wickramaratne, S.Z. Qiao, M. Jaroniec, Molecular-based design and emerging applications of nanoporous carbon spheres, Nat. Mater. 14 (2015) 763.
[7] S. Zheng, J. Zhang, H. Deng, Y. Du, X. Shi, Chitin derived nitrogen-doped porous carbons with ultrahigh specific surface area and tailored hierarchical porosity for high performance supercapacitors, J. Bioresour. Bioprod. 6 (2) (2021) 142–151.
[8] B. Yan, J. Zheng, F. Wang, L. Zhao, Q. Zhang, W. Xu, S. He, Review on porous carbon materials engineered by ZnO templates: design, synthesis and capacitance performance, Mater. Des. 201 (2021) 109518.
[9] C. Wang, B. Yan, Z. Chen, B. You, T. Liao, Q. Zhang, Y. Lu, S. Jiang, S. He, Recent advances in carbon substrate supported nonprecious nanoarrays for electrocatalytic oxygen evolution, J. Mater. Chem. A 9 (46) (2021) 25773–25795.
[10] S. Xiao, L. Hu, X. Pang, S. Li, Synthesis of a novel mesoporous carbon Nanocube@Mesoporous Silica@Poly(acrylic acid) composite and application as potential drug carriers, Russ. J. Phys. Chem. A 93 (7) (2019) 1349–1356.
[11] P. Liu, Y.L. Cao, C.X. Wang, X.Y. Chen, G.W. Yang, Micro- and nanocubes of carbon with C8-like and blue luminescence, Nano Lett. 8 (8) (2008) 2570–2575.
[12] R. Qiang, Y. Du, H. Zhao, Y. Wang, C. Tian, Z. Li, X. Han, P. Xu, Metal organic framework-derived Fe/C nanocubes toward efficient microwave absorption, J. Mater. Chem. A 3 (25) (2015) 13426–13434.
[13] V. Srinivasan, A. Kathiravan, M. Kathiresan, G. Krishnan, M.A. Jhonsi, Facile synthesis of carbon nanocubes and its applications for sensing antibiotics, J. Photochem. Photobiol. Chem. 403 (2020) 112855.
[14] M.-S. Wu, H.-C. Shih, J.-C. Lin, High-performance counter electrode of carbon nanocubes with embedded cobalt-iron alloy nanoparticles for dye-sensitized solar cells, Electrochim. Acta 279 (2018) 231–240.
[15] L. Zhu, Z. Wang, L. Wang, L. Xie, J. Li, X. Cao, ZnSe embedded in N-doped carbon nanocubes as anode materials for high-performance Li-ion batteries, Chem. Eng. J. 364 (2019) 503–513.
[16] Y. Li, X. Liang, G. Chen, W. Zhong, Q. Deng, F. Zheng, C. Yang, M. Liu, J. Hu, In-situ constructing Na3V2(PO4)2F3/carbon nanocubes for fast ion diffusion with high-performance Na+-storage, Chem. Eng. J. 387 (2020) 123952.
[17] S. Chen, B. Sun, X. Xie, A.K. Mondal, X. Huang, G. Wang, Multi-chambered micro/mesoporous carbon nanocubes as new polysulfides reserviors for lithium-sulfur batteries with long cycle life, Nano Energy 16 (2015) 268–280.
[18] J. Xi, Y. Xia, Y. Xu, J. Xiao, S. Wang, (Fe,Co)@nitrogen-doped graphitic carbon nanocubes derived from polydopamine-encapsulated metal–organic frameworks as a highly stable and selective non-precious oxygen reduction electrocatalyst, Chem. Commun. 51 (52) (2015) 10479–10482.
[19] Y.V. Lim, Y. Wang, D. Kong, L. Guo, J.I. Wong, L.K. Ang, H.Y. Yang, Cubic-shaped WS2 nanopetals on a Prussian blue derived nitrogen-doped carbon nanoporous framework for high performance sodium-ion batteries, J. Mater. Chem. A 5 (21) (2017) 10406–10415.
[20] C.M. Mani, M. Braun, V. Molinari, M. Antonietti, N. Fechler, A high-throughput composite catalyst based on nickel carbon cubes for the hydrogenation of 5-hydroxymethylfurfural to 2,5-dimethylfuran, ChemCatChem 9 (17) (2017) 3388–3394.
[21] C.M. Mani, T. Berthold, N. Fechler, "Cubism" on the nanoscale: from squaric acid to porous carbon cubes, Small 12 (21) (2016) 2906–2912.
[22] X. Hu, C. Wang, R. Luo, C. Liu, J. Qi, X. Sun, J. Shen, W. Han, L. Wang, J. Li, Double-shelled hollow ZnO/carbon nanocubes as an efficient solid-phase microextraction coating for the extraction of broad-spectrum pollutants, Nanoscale 11 (6) (2019) 2805–2811.
[23] A.P. Sgouros, G. Kalosakas, M.M. Sigalas, K. Papagelis, Exotic carbon nanostructures obtained through controllable defect engineering, RSC Adv. 5 (50) (2015) 39930–39937.
[24] S. Khodabakhhshi, P.F. Fulvio, A. Sousaraei, S. Kiani, Y. Niu, R.E. Palmer, W.C. H. Kuo, J. Rudd, A.R. Barron, E. Andreoli, Oxidative synthesis of yellow photoluminescent carbon nanoribbons from carbon black, Carbon 183 (2021) 495–503.
[25] J. Rouquerol, P. Llewellyn, F. Rouquerol, Is the bet equation applicable to microporous adsorbents? in: P.L. Llewellyn, F. Rodriquez-Reinoso, J. Rouqerol, N. Seaton (Eds.), Studies in Surface Science and Catalysis, 2007, pp. 49–56. Elsevier.
[26] M. Kruk, M. Jaroniec, Gas adsorption characterization of ordered organic-inorganic nanocomposite materials, Chem. Mater. 13 (10) (2001) 3169–3183.
[27] K. Kamegawa, K. Nishikubo, H. Yoshida, Oxidative degradation of carbon blacks with nitric acid (I)—changes in pore and crystallographic structures, Carbon 36 (4) (1998) 433–441.
[28] C.Y. Liu, W.T. Cheng, Surface modification and characterization of carbon black through oxidation, Surf. Interface Anal. 51 (3) (2019) 316–325.
[29] M. Singh, R.L. Vander Wal, Nanostructure quantification of carbon blacks, C 5 (1) (2019).
[30] A.K. Geim, K.S. Novoselov, The rise of graphene, Nat. Mater. 6 (3) (2007) 183–191.
[31] M.T. Lusk, D.T. Wu, L.D. Carr, Graphene nanoengineering and the inverse Stone-Thrower-Wales defect, Phys. Rev. B 81 (15) (2010) 155444.
[32] A.J. Stone, D.J. Wales, Theoretical studies of icosahedral C60 and some related species, Chem. Phys. Lett. 128 (5–6) (1986) 501–503.
[33] S. Khodabakhshi, P.F. Fulvio, E. Andreoli, Carbon black reborn: structure and chemistry for renewable energy harnessing, Carbon 162 (2020) 604–649.
[34] J. Guo, J.R. Morris, Y. Ihm, C.I. Contescu, N.C. Gallego, G. Duscher, S. J. Pennycook, M.F. Chisholm, Topological defects: origin of nanopores and enhanced adsorption performance in nanoporous carbon, Small 8 (21) (2012) 3283–3288.
[35] S. Khodabakhshi, S. Kiani, Y. Niu, A.O. White, W. Suwaileh, R.E. Palmer, A. R. Barron, E. Andreoli, Facile and environmentally friendly synthesis of ultramicroporous carbon spheres: a significant improvement in CVD method, Carbon 171 (2021) 426–436.
[36] S. Khodabakhshi, M. Taddei, J.A. Rudd, M.J. McPherson, Y. Niu, R.E. Palmer, A. R. Barron, E. Andreoli, Interplay between oxygen doping and ultra-microporosity improves the CO2/N2 separation performance of carbons derived from aromatic polycarboxylates, Carbon 173 (2021) 989–1002.
[37] M.A. Lillo-Ródenas, D. Cazorla-Amorós, A. Linares-Solano, Understanding chemical reactions between carbons and NaOH and KOH: an insight into the chemical activation mechanism, Carbon 41 (2) (2003) 267–275.
[38] Z.Q. Li, C.J. Lu, Z.P. Xia, Y. Zhou, Z. Luo, X-ray diffraction patterns of graphite and turbostratic carbon, Carbon 45 (8) (2007) 1686–1695.
[39] J.A. Rudd, D.R. Jones, C.W. Dunnill, E. Andreoli, Study of copper(II) oxide and copper(II) acetate on multiwalled carbon nanotubes by XPS, Surf. Sci. Spectra 26 (1) (2019).
[40] J. Taráabek, L. Kavan, L. Dunsch, M. Kalbac, Chemical states of electrochemically doped single wall carbon nanotubes as probed by Raman spectroelectrochemistry and ex situ X-ray photoelectron spectroscopy, J. Phys. Chem. C 112 (36) (2008) 13856–13861.
[41] G. Greczynski, L. Hultman, Reliable determination of chemical state in x-ray photoelectron spectroscopy based on sample-work-function referencing to adventitious carbon: resolving the myth of apparent constant binding energy of the C 1s peak, Appl. Surf. Sci. 451 (2018) 99–103.
[42] Y. Zhai, Y. Dou, D. Zhao, P.F. Fulvio, R.T. Mayes, S. Dai, Carbon materials for chemical capacitive energy storage, Adv. Mater. 23 (42) (2011) 4828–4850.
[43] C. Liu, F. Li, L.-P. Ma, H.-M. Cheng, Advanced materials for energy storage, Adv. Mater. 22 (8) (2010) E28–E62.
[44] A.A. Abd, M.R. Othman, J. Kim, A review on application of activated carbons for carbon dioxide capture: present performance, preparation, and surface modification for further improvement, Environ. Sci. Pollut. Control Ser. 28 (32) (2021) 43329–43364.
[45] G. Singh, K.S. Lakhi, S. Sil, S.V. Bhosale, I. Kim, K. Albahily, A. Vinu, Biomass derived porous carbon for CO2 capture, Carbon 148 (2019) 164–186.
[46] T.C. Merkel, H. Lin, X. Wei, R. Baker, Power plant post-combustion carbon dioxide capture: an opportunity for membranes, J. Membr. Sci. 359 (1–2) (2010) 126–139.
[47] M. Sevilla, J.B. Parra, A.B. Fuertes, Assessment of the role of micropore size and N-doping in CO2 capture by porous carbons, ACS Appl. Mater. Interfaces 5 (13) (2013) 6360–6368.
[48] N.P. Wickramaratne, M. Jaroniec, Importance of small micropores in CO2 capture by phenolic resin-based activated carbon spheres, J. Mater. Chem. A 1 (1) (2013) 112–116.
[49] J. Serafin, U. Narkiewicz, A.W. Morawski, R.J. Wróbel, B. Michalkiewicz, Highly microporous activated carbons from biomass for CO2 capture and effective micropores at different conditions, J. CO2 Util. 18 (2017) 73–79.
[50] E. García-Díez, S. Schaefer, A. Sanchez-Sanchez, A. Celzard, V. Fierro, M. M. Maroto-Valer, S. García, Novel porous carbons derived from coal tar rejects: assessment of the role of pore texture in CO2 capture under realistic postcombustion operating temperatures, ACS Appl. Mater. Interfaces 11 (40) (2019) 36789–36799.

[51] K.S. Walton, D.S. Sholl, Predicting multicomponent adsorption: 50 years of the ideal adsorbed solution theory, AIChE J. 61 (9) (2015) 2757–2762.
[52] D. Saha, M.J. Kienbaum, Role of oxygen, nitrogen and sulfur functionalities on the surface of nanoporous carbons in CO2 adsorption: a critical review, Microporous Mesoporous Mater. 287 (2019) 29–55.
[53] N.P. Wickramaratne, J. Xu, M. Wang, L. Zhu, L. Dai, M. Jaroniec, Nitrogen enriched porous carbon spheres: attractive materials for supercapacitor electrodes and CO2 adsorption, Chem. Mater. 26 (9) (2014) 2820–2828.
[54] J. Liang, Q. Song, J. Lin, Y. Huang, Y. Fang, C. Yu, Y. Xue, Z. Liu, C. Tang, Pore structure regulation and carbon dioxide adsorption capacity improvement on porous BN fibers: effects of high-temperature treatments in gaseous ambient, Chem. Eng. J. 373 (2019) 616–623.
[55] S. Chowdhury, R. Balasubramanian, Holey graphene frameworks for highly selective post-combustion carbon capture, Sci. Rep. 6 (1) (2016) 21537.
[56] M. Wang, Z. Xu, J. Fu, H. Du, S. Wang, Effect of chemical activators on polyphosphazene-based hierarchical porous carbons and their good CO2 capture, Diam. Relat. Mater. 125 (2022) 108966.
[57] Y. Li, R. Xu, B. Wang, J. Wei, L. Wang, M. Shen, J. Yang, Enhanced N-doped porous carbon derived from KOH-activated waste wool: a promising material for selective adsorption of CO2/CH4 and CH4/N2, Nanomaterials 9 (2) (2019) 266.
[58] H. Wang, H. Wang, G. Liu, Q. Yan, In-situ pyrolysis of Taihu blue algae biomass as appealing porous carbon adsorbent for CO2 capture: role of the intrinsic N, Sci. Total Environ. 771 (2021) 145424.
[59] P. Yang, L. Rao, W. Zhu, L. Wang, R. Ma, F. Chen, G. Lin, X. Hu, Porous carbons derived from sustainable biomass via a facile one-step synthesis strategy as efficient CO2 adsorbents, Ind. Eng. Chem. Res. 59 (13) (2020) 6194–6201.
[60] Y. Li, T. Zhang, Y. Wang, B. Wang, Transformation of waste cornstalk into versatile porous carbon adsorbent for selective CO2 capture and efficient methanol adsorption, J. Environ. Chem. Eng. 9 (5) (2021) 106149.
[61] X. Guo, G. Zhang, C. Wu, J. Liu, G. Li, Y. Zhao, Y. Wang, Y. Xu, A cost-effective synthesis of heteroatom-doped porous carbon by sulfur-containing waste liquid treatment: as a promising adsorbent for CO2 capture, J. Environ. Chem. Eng. 9 (2) (2021) 105165.
[62] L. Vazhayal, P. Wilson, K. Prabhakaran, Utilization of waste aquatic weeds for the sustainable production of nitrogen doped nanoporous carbon for CO2 capture, Mater. Today: Proc. 52 (2022) 2315–2321.
[63] I.S. Ismail, G. Singh, P. Smith, S. Kim, J.-H. Yang, S. Joseph, S. Yusup, M. Singh, V. Bansal, S.N. Talapaneni, A. Vinu, Oxygen functionalized porous activated biocarbons with high surface area derived from grape marc for enhanced capture of CO2 at elevated-pressure, Carbon 160 (2020) 113–124.
[64] H. Cui, J. Xu, J. Shi, S. You, C. Zhang, N. Yan, Y. Liu, G. Chen, Evaluation of different potassium salts as activators for hierarchically porous carbons and their applications in CO2 adsorption, J. Colloid Interface Sci. 583 (2021) 40–49.
[65] C.R. Kagan, C.B. Murray, Charge transport in strongly coupled quantum dot solids, Nat. Nanotechnol. 10 (12) (2015) 1013–1026.
[66] D. Wang, M. Hermes, R. Kotni, Y. Wu, N. Tasios, Y. Liu, B. de Nijs, E.B. van der Wee, C.B. Murray, M. Dijkstra, A. van Blaaderen, Interplay between spherical confinement and particle shape on the self-assembly of rounded cubes, Nat. Commun. 9 (1) (2018) 2228.
[67] F. Su, Z. Tian, C.K. Poh, Z. Wang, S.H. Lim, Z. Liu, J. Lin, Pt nanoparticles supported on nitrogen-doped porous carbon nanospheres as an electrocatalyst for fuel cells, Chem. Mater. 22 (3) (2010) 832–839.
[68] N.P. Brandon, D.J. Brett, Engineering porous materials for fuel cell applications, Phil. Trans. Math. Phys. Eng. Sci. 364 (1838) (2006) 147–159.